nature communications

Article https://doi.org/10.1038/s41467-025-58300-9

Magnetotransport evidence for the coexistence of two-dimensional superconductivity and ferromagnetism at (111)-oriented a-$CaZrO_3$/$KTaO_3$ interfaces

Received: 31 July 2024

Accepted: 14 March 2025

Published online: 28 March 2025

Check for updates

Hui Zhang[1,12], Yinan Xiao[1,12], Qixuan Gao[2,12], Ning Wu[3,4,12], Siyi Zhou[2], Yongchao Wang[2], Mengqin Wang[5,6], Daming Tian[1], Lu Chen[1], Weijian Qi[1], Dongyao Zheng[1], Jine Zhang[1], Furong Han[1], Huaiwen Yang[1], Banggui Liu[5,6], Yuansha Chen[5,6], Fengxia Hu[5,6,7], Baogen Shen[5,6,8], Jirong Sun[5,9], Weisheng Zhao[1] & Jinsong Zhang[2,10,11]

Exploring the intricate interplay between magnetism and superconductivity is crucial for unveiling the underlying mechanisms of unconventional superconductivity. Here, we report on the magnetotransport evidence for the coexistence of a two-dimensional (2D) superconducting state and a 2D ferromagnetic state at the interface between amorphous $CaZrO_3$ film and (111)-oriented $KTaO_3$ single crystal. Remarkably, the fingerprint of ferromagnetism, i.e., hysteretic magnetoresistance loops, is observed in the superconducting state. The butterfly-shaped hysteresis with twin peaks emerges against the background of superconducting zero resistance, and the peak amplitude increases with the sweep rate of the magnetic field, indicating that the magnetization dynamics are at play in the superconducting state. Moreover, the magnetoresistance hysteresis is strongly dependent on temperature, achieving a maximum near the superconducting transition temperature. This behavior is well described by the thermal activated phase slip model. Density function theory (DFT) calculations suggest that the magnetic moment is primarily contributed by the Ta $5d_{yz}$ orbital, and the Stoner ferromagnetism is identified. Our findings provide new insights into the interaction of magnetism and superconductivity at $KTaO_3$-based oxide heterointerfaces.

Interfaces with inversion symmetry breaking present new avenues for electron pairing, providing a valuable platform for exploring the emergent quantum phenomena associated with unconventional superconductivity[1–3]. The most prominent example is the superconducting interface between two insulating oxides $LaAlO_3$ (LAO) and $SrTiO_3$ (STO)[4]. In addition to the two-dimensional (2D) superconductivity, the coexisted ferromagnetism at this interface has also been unveiled by high-resolution magnetic torque magnetometry[5], scanning superconducting quantum interference device (SQUID)[6], and magnetoresistance[7]. The magnetic exchange is considered to be a key ingredient of high-temperature superconductivity, and the formation of unconventional superconducting pairs is closely related to magnetism[8–10]. Obviously, 2D oxide heterointerfaces provide opportunities for exploring the underlying physics of unconventional

A full list of affiliations appears at the end of the paper. e-mail: huizh@buaa.edu.cn; jrsun@iphy.ac.cn; wszhao@buaa.edu.cn; jinsongzhang@mail.tsinghua.edu.cn

 https://doi.org/10.1038/s41467-025-58300-9

superconductivity. However, the extremely low superconducting critical temperature T_C (below 250 mK) of the STO-based 2D electron gases (2DEGs)[1,11,12] limits a thorough investigation of the superconductivity-magnetism correlation.

The recent discovery of superconducting 2DEGs at the $KTaO_3$ (KTO)-based heterointerfaces has attracted much attention because its T_C is up to ~2 K[13–17], nearly an order of magnitude higher than that of STO. KTO is in many ways similar to STO. However, the 2DEGs residing in KTO derive from 5*d* orbitals rather than 3*d* orbitals, exhibiting a large atomic spin-orbit coupling (SOC) and unique properties compared to the 2DEGs in STO[18]. For example, the superconductivity of KTO-based 2DEGs is strongly dependent on crystal orientation[15–17,19–21], a feature that is absent in the STO system[1,11,12]. Although the 2DEGs at KTO interfaces with (001) crystal orientation exhibit no interfacial superconductivity down to 25 mK[15,16], higher transition temperatures up to 0.9 and 2.2 K were observed for samples oriented along (110)[20] and (111)[17], respectively. These results indicate that the superconductivity could be closely related to the interfacial *d*-orbital reconstruction[22]. Meanwhile, an admixture of *s*-wave and *p*-wave pairing components induced by strong SOC has been revealed in KTO-based 2DEG[14]. In principle, the integration of strong SOC, superconductivity and long-range ferromagnetic (FM) order could potentially realize the long-sought-after spin-triplet pairing and topological superconductivity[23–28]. We note that the KTO interface has already demonstrated strong SOC and 2D superconductivity, thus it is of great significance to explore the long-range ferromagnetism that coexists with superconductivity. Very recently, magnetization hysteresis loops were observed for the (111)-AM/KTO interfaces over a wide temperature range from 1.8 to 300 K (AM denotes $LaAlO_3$ or $YAlO_3$ amorphous films)[29], suggesting coexisted superconductivity and ferromagnetism noting that 1.8 K is slightly lower than the onset temperature of the superconductivity investigated there. However, direct magnetotransport evidences are lacking, especially when the system is in the well-superconducting state at extremely low temperatures. Here, we present magnetotransport evidences for the coexistence of 2D superconductivity and 2D ferromagnetism over a wide temperature range for (111)-oriented a-CZO/KTO interfaces (CZO=$CaZrO_3$ and a-CZO denotes amorphous CZO film). As experimentally demonstrated, butterfly-shaped magnetoresistance (MR) emerges when temperature is lower than the superconducting onset temperature, achieves a peak value around T_C, and decreases rapidly with the further decrease of temperature. However, MR remains sizable even at the temperature of 0.05 K which is well below the zero-resistance temperature, indicating the concomitant occurrence of magnetic ordering and superconducting. A rapid increase of the hysteretic MR with the sweep rate of the magnetic field is further observed while fixing the temperature at a constant value, providing a conclusive proof that the magnetization dynamics are at play in the superconducting state. Density functional theory (DFT) calculations show that oxygen vacancy-induced gap states cause an increase in the density of states (DOS) near the Fermi surface, inducing the itinerant FM state according to the Stoner model.

Results and discussion

Amorphous CZO films, 10 nm in thickness, were grown on (111)-oriented KTO single crystal substrates by pulsed laser deposition (PLD). The surface morphology of the film is atomically flat (Fig. S1). The microstructure of the heterointerface was assessed by the technique of high-resolution scanning transmission electron microscopy (STEM). The typical high-angle annular dark-field (HAADF) image of the a-CZO/KTO(111) cross-section, recorded along the [1-10] zone axis of KTO is shown in Fig. 1a. A large-scale HAADF-STEM image is shown in

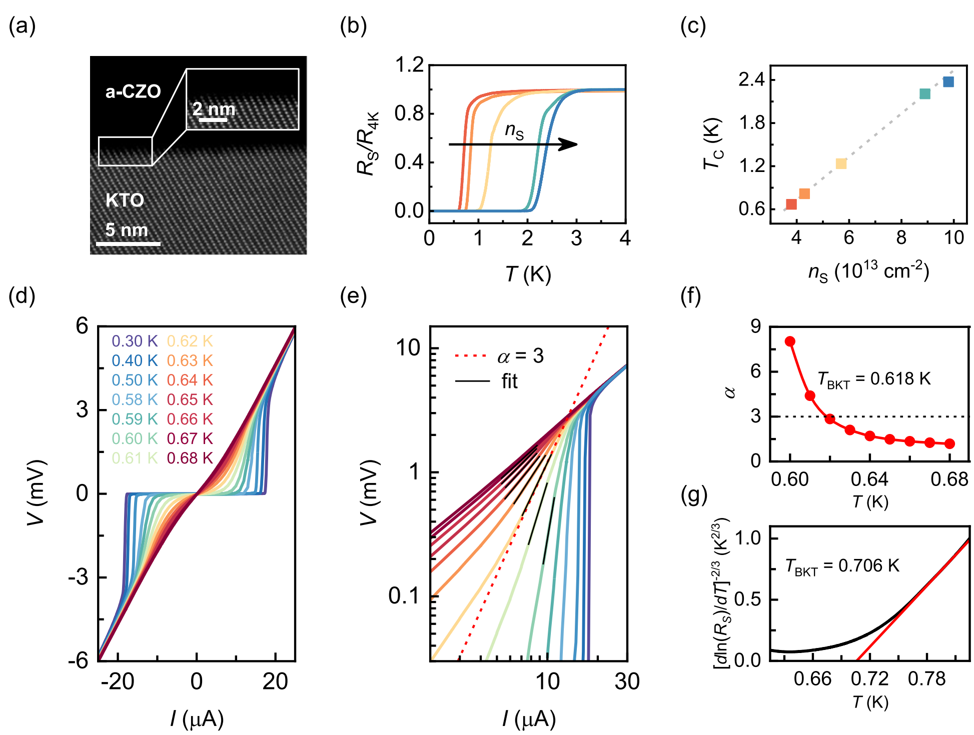

Fig. 1 | Two-dimensional superconductivity at a-CZO/KTO(111) interface. **a** HAADF-STEM image of a-CZO/KTO(111) heterostructure measured along [1-10] zone axis, showing that the CZO film is amorphous. **b** R_S/R_{4K} as a function of temperature for samples with different carrier densities n_S, where R_{4K} is the normal-state resistance at 4 K. The direction of the arrow indicates the increase of n_S, which grows from 3.8×10^{13} to 9.8×10^{13} cm^{-2}. **c** n_S dependence of T_C, where T_C is determined at 50% of R_{4K}. The dashed line is a guide for the eyes. **d** Temperature-dependent *I*–*V* measurements for sample with $n_S = 3.8 \times 10^{13}$ cm^{-2}. **e** *I*–*V* curves plotted on a logarithmic scale with the same color codes as in (**d**). The Red dashed line represents $V \propto I^{\beta}$, which is used to infer the BKT transition temperature. **f** Temperature dependence of the power-law exponent α, as deduced from the linear fits of the curves in (**e**). **g** Sheet resistance dependence of temperature plotted on a $[d\ln(R_S)/dT]^{-2/3}$ scale. The red solid line is a linear extrapolation from the high-*T* linear section, which crosses the *T*-axis at $T_{BKT} = 0.706$ K.

Fig. S2. Structural characterization indicates that the CZO film is amorphous and homogeneous, and the a-CZO/KTO interface is abrupt and smooth. A close inspection of the lattice image indicates a slight blurring in color contrast within an interfacial layer of ~0.5 nm at the a-CZO/KTO interface, which could be attributed to the deficiency of oxygen near the interface. Additionally, X-ray photoelectron spectroscopy (XPS) measurements indicate the presence of Ta^{4+} ions with a content of 22.8% (see Fig. S3 and Table S1), suggesting the occurrence of oxygen vacancies which could be introduced into the KTO substrate by the PLD deposition of the a-CZO film. Notably, oxygen vacancies act as electron donors, contributing charge carriers to the 2DEGs at the a-CZO/KTO interfaces.

By adjusting the growth parameters, metallic 2DEGs with different carrier densities (n_S) were obtained, as detailed in the Methods section and Table S2. The carrier density increases as the oxygen pressure for PLD decreases, lateral evidence for the existence of oxygen vacancies. Figure 1b shows the temperature dependence of the reduced sheet resistance R_S/R_{4K} (R_{4K} is the normal-state resistance at 4 K) for the sample with a n_S between 3.8×10^{13} and $9.8 \times 10^{13}\ \mathrm{cm}^{-2}$, where n_S is deduced from the Hall effect of 10 K (Fig. S4). The superconductivity can be clearly seen for all samples, and the superconducting transition temperature T_C, defined by the temperature corresponding to $R_{4K}/2$, shows a strong dependence on carrier density. It exhibits a linear increase with n_S with a T_C–n_S slope of ~2.84×10^{-14} K•cm^2 (Fig. 1c). A similar relation between T_C and n_S was also found for the 2DEGs at the EuO/KTO(111)[15] and AlO_x/KTO(111)[13] interfaces, displaying a T_C–n_S slope reduced by ~20%. Remarkably, T_C is as high as ~2.4 K in our 2DEG with $n_S = 9.8 \times 10^{13}\ \mathrm{cm}^{-2}$, nearly 12 times higher than that in the LAO/STO system[1].

The Berezinskii–Kosterlitz–Thouless (BKT) transition is a typical behavior of the 2D superconducting systems, characterized by a $V \propto I^{\alpha}$ power-law relation with $\alpha = 3$ at the transition temperature[1,30], where I and V are applied current and corresponding voltage, respectively. To get an idea about the BKT transition, Fig. 1d presents the I–V characteristics acquired at different temperatures for the sample with $n_S = 3.8 \times 10^{13}\ \mathrm{cm}^{-2}$. By linearly fitting the logarithmically scaled I–V relation (Fig. 1e, f), we found a T_{BKT} of ~0.618 K, corresponding to the exponent α of 3. In addition, the T_{BKT} can also be estimated from the formula $R_S(T) = R_0\exp[-b(T/T_{BKT}-1)^{-1/2}]$, where R_0 and b are material parameters[31]. Application of such a fit to the $R_S(T)$ curve suggests $T_{BKT} = 0.706$ K for the sample of $n_S = 3.8 \times 10^{13}\ \mathrm{cm}^{-2}$ (Fig. 1g), consistent with the corresponding result obtained from the analysis of the I–V characteristics. A similar analysis for the sample with $n_S = 9.8 \times 10^{13}\ \mathrm{cm}^{-2}$ is shown in Fig. S5, and T_{BKT} of ~2.153 K and 2.078 K are obtained from the analysis of the α exponent and the fit to the $R_S(T)$ curve, respectively. These results confirm the 2D nature of the superconductivity at the a-CZO/KTO(111) interfaces.

To reveal the effect of magnetic field on superconductivity, we measured the reduced resistances $R_S/R_{0.5T}$ and R_S/R_{8T} with out-of-plane field ($\mu_0 H_{\perp}$) and in-plane magnetic field ($\mu_0 H_{||}$), respectively, for the sample of $n_S = 3.8 \times 10^{13}\ \mathrm{cm}^{-2}$ at different temperatures, and the corresponding results are shown in Fig. 2a, b. From the data in Fig. 2a, b, the upper critical field can be deduced. Figure 2c illustrates the temperature dependence of the upper critical fields $\mu_0 H_{C2\perp}$ and $\mu_0 H_{C2||}$, defined by the half normal-state resistances $R_{0.5T}$ and R_{8T}, respectively. We further performed an analysis of the $\mu_0 H_{C2}$–T relation based on the Ginzburg–Landau theory[32]:

$$\mu_0 H_{C2\perp} = [\varphi_0/2\pi\xi_{GL}^2(0)]\left(1-\frac{T}{T_C}\right) \quad (1)$$

$$\mu_0 H_{C2||} = [\varphi_0\sqrt{12}/2\pi\xi_{GL}(0)d_{SC}]\left(1-\frac{T}{T_C}\right)^{1/2} \quad (2)$$

where φ_0 is the magnetic flux quantum, and d_{SC} is the superconducting layer thickness. Fitting the experiment data to Eqs. (1) and (2) leads to the zero-temperature limit $\mu_0 H_{C2\perp}(0) = 0.09$ T and $\mu_0 H_{C2||}(0) = 3.99$ T, indicating a large anisotropic ratio of ~44, and the coherence length $\xi_{GL}(0) = 61.63$ nm more than 13 times larger than $d_{SC} = 4.63$ nm. These results reconfirm the 2D characteristics of the superconductivity. In addition, the mean free path l_{mfp} of the conducting electrons can be estimated using $l_{mfp} = (h/e^2)(1/k_F R_S)$, where $k_F = (2\pi n_S)^{1/2}$ and h are the Fermi wave number and Planck constant, respectively[30]. Adopting the n_S and R_S obtained at $T = 10$ K, the l_{mfp} of the present 2DEG is found to be ~12.3 nm, which is about 20% of ξ_{GL}. Therefore, the superconductivity at the a-CZO/KTO(111) interface occurs in an intermediate range between clean ($l_{mfp} \gg \xi_{GL}$) and dirty ($l_{mfp} \ll \xi_{GL}$) limits, which is similar to a-LAO/KTO(110)[20] and EuO/KTO(111)[15], but different from EuO/KTO(110) for which $l_{mfp} > \xi_{GL}$[33]. For weakly coupled BCS superconductors, the Pauli paramagnetic limit acts as the theoretical upper bound for the parallel critical field[34,35], which is given by $\mu_0 H_{C2}^P \approx 1.76 k_B T_C/\sqrt{2}\mu_B$, where μ_B is Bohr magneton. Taking $T_C = 0.668$ K, we obtain $\mu_0 H_{C2}^P = 1.24$ T (a red solid circle in Fig. 2c), which is only 31% of the measured $\mu_0 H_{C2||}(0) = 3.99$ T. Obviously, the Pauli paramagnetic limit is drastically exceeded. To clarify the origins of the large $\mu_0 H_{C2||}$, we systematically investigated the back gating effect for the a-CZO/KTO(111) sample with $n_S = 3.8 \times 10^{13}\ \mathrm{cm}^{-2}$, which corresponds to the n_S value of the as-grown sample (Note 1 and Fig. S6). The carrier density n_S can be tuned by applying the gate voltage V_G. The dependence of $\mu_0 H_{C2||}$ on n_S is obtained, indicating that $\mu_0 H_{C2||}$ increases from 3.6 to 5.0 T as n_S decreases from $3.8 \times 10^{13}\ \mathrm{cm}^{-2}$ to $2.9 \times 10^{13}\ \mathrm{cm}^{-2}$ (Fig. S6g). Note that a higher $\mu_0 H_{C2||}$ is observed in the a-CZO/KTO(111) system compared to LAO/STO (111) systems (~4.5 T)[40]. The analysis of the n_S-dependent spin-orbit energy ε_{so} reveals that ε_{so} increases as n_S decreases (Fig. S6i), which is consistent with the variation of $\mu_0 H_{C2||}$ with n_S. Therefore, the high $\mu_0 H_{C2||}$ value exceeding the Pauli limit could be attributed to the strong SOC of the $5d$ 2DEG at KTO-based interfaces, which stems from the inversion symmetry breaking at the a-CZO/KTO interface and the presence of relatively heavy tantalum ions[18,36–39].

Strikingly, sharp resistance peaks are observed in the low-field range of the R_S/R_{8T}–$\mu_0 H_{||}$ curves collected at low temperatures (Fig. 2b), suggesting a deviation of the transport behavior from superconductivity. The resistance peaks can be clearly seen in a magnified view of the low-field data (Fig. S7). To get further knowledge about this resistive anomaly, the resistance is re-measured by sweeping $\mu_0 H_{||}$ in a narrow field range between −1.5 and 1.5 T. Figure 2d shows the reduced resistance recorded with the $\mu_0 H_{||}$ parallel to applied current I at several typical temperatures (the R_S/R_{8T}–$\mu_0 H_{||}$ curves have been vertically shifted for clarity). The most remarkable observation is the magnetic hysteresis in the superconducting background, as indicated by the appearance of butterfly-shaped R_S/R_{8T}–$\mu_0 H_{||}$ curves. This is a signature of magnetic ordering as will be discussed in detail later. Further analysis shows that the resistive anomaly is robust. Hysteretic MR loops occur no matter $\mu_0 H_{||}$ is parallel or perpendicular to the applied current (Fig. 2e). Applying current along [11-2] or [1-10] crystal orientations also lead to magnetic hysteresis (Fig. S8). It is therefore a general feature of the magnetotransport behaviors of the a-CZO/KTO interface. Moreover, MR peaks appear over a wide temperature range, covering both the superconducting state ($T < T_C$) and the normal state ($T > T_C$) (Fig. S7). The magnetism in the normal state can also be confirmed by the magnetization dependence on the magnetic field, measured using the SQUID. The ferromagnetic hysteresis loops at various temperatures clearly demonstrate the persistence of normal-state magnetism up to room temperature (Fig. S9), consistent with the findings reported in ref. 29. The undetectability of the MR loop at higher temperatures could be attributed to the precision limitations of the magnetotransport system.

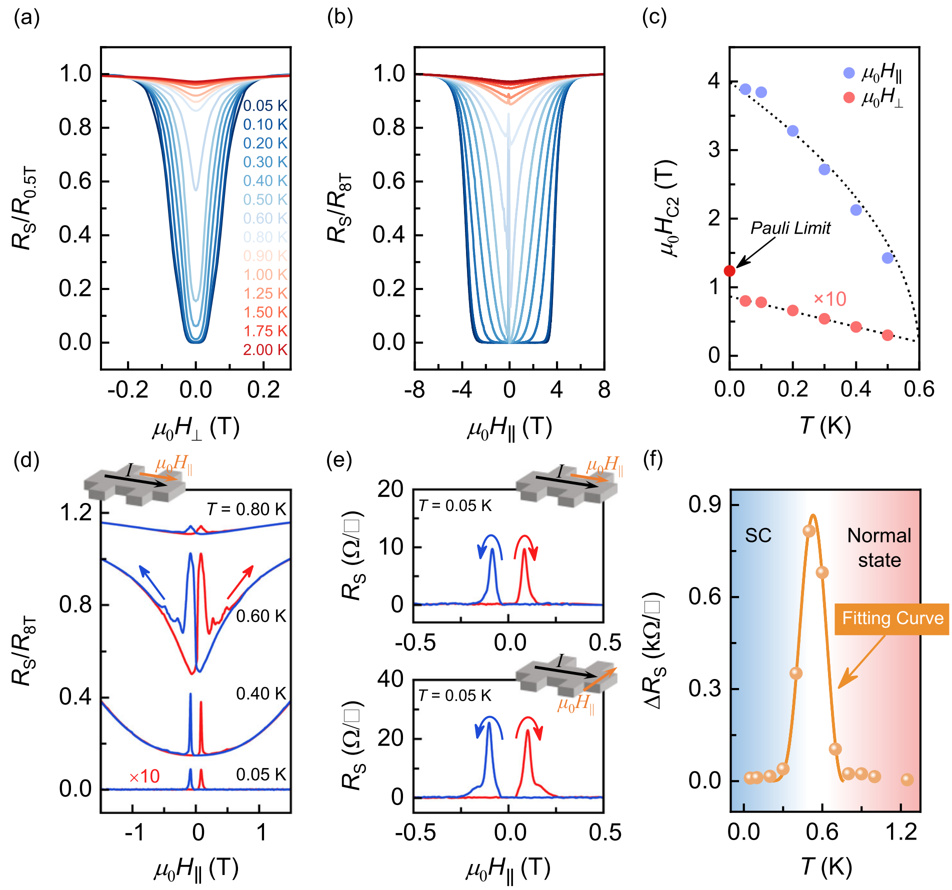

Fig. 2 | MR loops in superconducting state. a $R_S/R_{0.5T}$ as a function of the out-of-plane magnetic field at different temperatures ranging from 0.03 to 2 K, where $R_{0.5T}$ is the normal-state resistance when $\mu_0H_\perp = 0.5$ T. **b** In-plane magnetic field dependence of R_S/R_{8T}, where R_{8T} is the normal-state resistance when $\mu_0H_\parallel = 8$ T. The symbol label is the same as that in (**a**). **c** Temperature dependence of the upper critical field μ_0H_{C2}, derived from half of the normal-state resistance. Dashed lines are fitting curves based on Ginzburg–Landau theory. The estimated Pauli paramagnetic limit is marked with a red dot. **d** R_S/R_{8T} as a function of $\mu_0H_\parallel$ at different temperatures. Blue and red arrows indicate the direction of the field sweep. The upper left corner shows the geometry for the measurements. **e** In-plane magnetoresistance at 0.05 K with the magnetic field parallel or perpendicular to applied current. The upper right corners indicate the measurement geometries. **f** Temperature dependence of the difference in sheet resistance, denoted as $\Delta R_S = R_S(\mu_0H_\parallel = 0.08\ \mathrm{T}) - R_S(\mu_0H_\parallel = 0)$. The marks represent the experimental data. The solid line is fitted using the LAMH theory for TAPS.

To get a quantitative description about the thermal evolution of the butterfly-shaped R_S/R_{8T}–$\mu_0H_\parallel$ behavior, in Fig. 2f we show the peak resistance, defined by $\Delta R_S = R_S(\mu_0H_\parallel = 0.08\ \mathrm{T})$-$R_S(\mu_0H_\parallel = 0)$, as a function of temperature. Here $\mu_0H_\parallel = 0.08$ T is the position of resistance peaks. As shown in Fig. 2f, ΔR_S is low at high temperatures, rapidly increases with the decrease of temperature, and gets the maximum value ~ 814.9 ohms/square (Ω/□) at ~ 0.5 K, a temperature slightly lower than the zero-resistance temperature (~0.6 K). Further cooling results in a drastic decrease in ΔR_S. However, ΔR_S remains identifiable even at the temperatures well below T_C. It is, for example, ~9.7 Ω/□ at 0.05 K where the system is expected to be in the well-superconducting state. The implications of these results are twofold. The first one is the concomitant occurrence of the FM phase and superconducting phase, as suggested by the considerable MR peaks at temperatures well below T_C, and the second one is the strong competition between magnetic ordering and superconducting, as implied by the occurrence of the strongest MR effect close to the zero-resistance temperature at which a percolation of the superconducting phase may just take place. An explanation for this peak behavior of ΔR_S will be presented later.

Magnetic hysteresis MR has been reported for the superconducting 2DEG at the LAO/STO interface, and ascribed to the effect of vortex moving[41]. It was also observed in normal-state 2DEG at the EuO/KTO interface[33], and attributed to the magnetic proximity effect of the FM EuO over layer on 2DEG[42,43]. However, this phenomenon was never observed before in the superconducting 2DEG at the KTO-based interfaces.

In general, the occurrence of magnetic hysteresis is a signature of the existence of magnetic domains. As well documented[42], a resistance peak emerges when magnetic domains change their polarities as the magnetic field sweeps through coercive field; the structure of the magnetic domains is most disordered at the coercive field and, correspondingly, the resistance is maximal due to enhanced magnetic scattering. It is a typical feature of metallic magnetic materials that MR peaks at coercive field.

The magnetotransport process in superconductors may be somewhat different from that in normal conductors. When the system enters the superconducting state, the onset of superconducting pairing could induce a granular superconductor[44]. Given the impact of the domain wall of the ferromagnet on superconductivity, the magnetization dynamics in the ferromagnet will generate moving vortices in the superconductor as $\mu_0H_\parallel$ sweeps[41]. Notably, the intermediate areas between adjacent superconducting grains can enclose magnetic vortices. In this case, the motion of the magnetic vortices will cause an increase in resistance as the vortices cross the weak links between superconducting grains[41,44]. When the system is cooled well below T_C, the superconducting islands expand and merge with each other, forming percolated superconducting areas that dominate the transport behavior of the 2DEGs. As the intermediate region between the

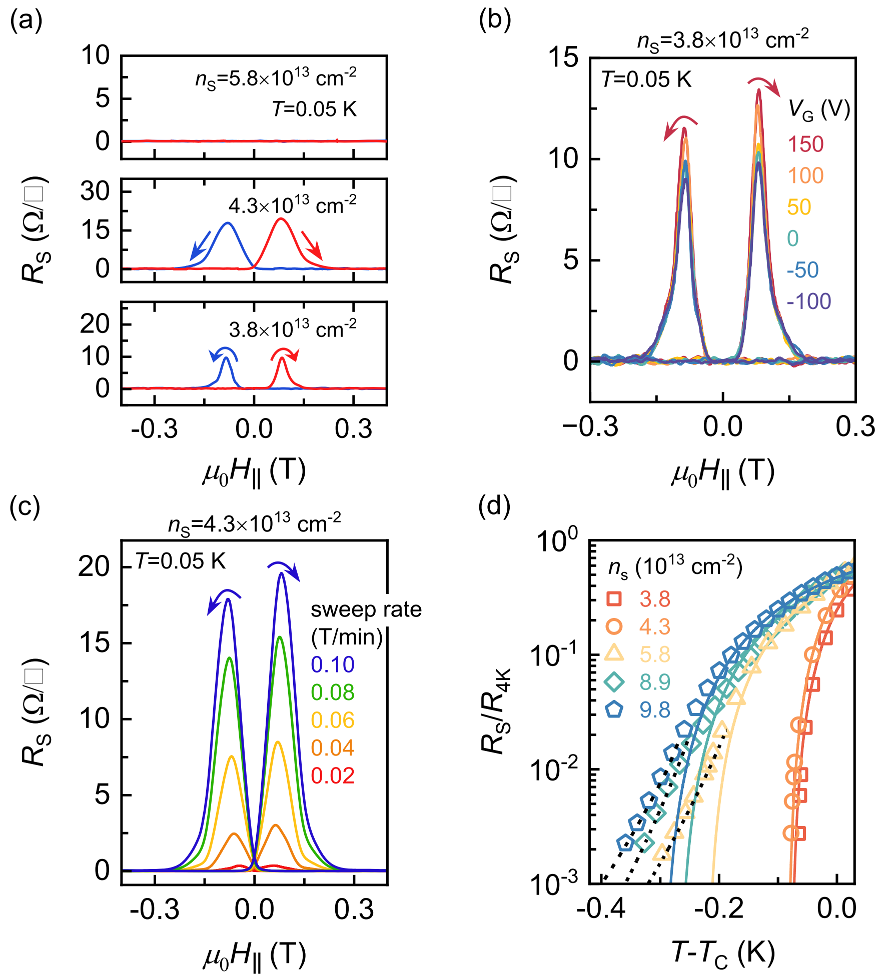

Fig. 3 | Hysteresis induced by the magnetization dynamics. a In-plane magnetoresistance for samples with different carrier density at 0.05 K. **b** In-plane magnetoresistance at different V_G values measured at 0.05 K for the sample with $n_S = 3.8 \times 10^{13}$ cm^{-2}, which corresponds to the n_S value of the as-grown sample. **c** In-plane magnetoresistance at different field sweep rates for $n_S = 4.3 \times 10^{13}$ cm^{-2} at 0.05 K. **d** R_S/R_{4K} as a function of normalized temperature $T-T_C$. The marks represent the experimental data. The solid lines and dashed black lines are fitting curves using the LAMH theory for TAPS and the Golubev–Zaikin model for QPS, respectively. The hollow patterns indicate the values of carrier densities.

interconnected islands shrinks, the resistance effect induced by the vortex moving across these junctions is quickly weakened, which is in good agreement with the reduction in the MR peak amplitude with decreasing temperature. Note that a finite resistance peak observed at $T = 0.05$ K clearly verifies that the dissipationless energy transfer in superconductors has been disrupted by vortex motion.

Obviously, the proportion of the weakly linked area between superconducting grains determines the size of the hysteretic MR peaks. With the decrease of this proportion, the MR peak is expected to diminish and, finally, vanish when superconducting areas dominate the transport behavior of the 2DEG. Considering the close relation between superconductivity and carrier density shown in Fig. 1b, c, we further investigated the influence of n_S on the R_S–$\mu_0 H_{||}$ loops measured at 0.05 K by applying a magnetic field parallel to current (Figs. 3a and S10). The dependence of the peak resistance ΔR_S on carrier density is shown in Fig. S11. As the doping level grows from 3.8×10^{13} to 4.3×10^{13} cm^{-2}, the peak value of the resistance increases from ~9.7 to ~19.6 Ω/□. However, the resistance peak vanishes when n_S exceeds 5×10^{13} cm^{-2}, leaving a zero-resistance background. To explore the role of disorder, the mean free path l_{mfp} is plotted as a function of n_S (Fig. S11). The results indicate that l_{mfp} does not exhibit a significant dependence on n_S. Obviously, the disorder mechanism cannot account for the disappearance of the resistivity peak at densities above 5×10^{13} cm^{-2}. The butterfly-shaped hysteresis could be attributed to the vortex motion across the weak links between superconducting grains. At low n_S, superconducting islands are sparsely distributed in a non-superconducting background. In this case, the small number of interconnected islands results in a weak resistance effect when the vortex moves across these junctions, consistent with the small magnitude of ΔR_S. As n_S increases, the sample enters into a deeper superconducting state due to the higher T_C, which means that the superconducting islands expand and form more interconnected islands. The increase in the proportion of the weakly linked area leads to an increase in ΔR_S. However, when n_S further increases, crossing the percolation threshold, the continued growth and merging of superconducting islands cause the weakly linked regions to be short-circuited by the superconducting phase, resulting in a dropping of ΔR_S to zero. Thus, the disappearance of the resistivity peak at carrier densities above 5×10^{13} cm^{-2} could be attributed to the percolation of the superconducting phases.

As mentioned earlier, the back gating effect for the a-CZO/KTO(111) sample with $n_S = 3.8 \times 10^{13}$ cm^{-2}, corresponding to the n_S value of the as-grown sample, has been investigated (Fig. S6). Figure 3b plots the peak resistance ΔR_S as a function of the back gate voltage V_G. Notably, as V_G changes from +150 V to −100 V, ΔR_S decreases from 13.4 to 9.8 Ω/□, and l_{mfp} decreases from 13.7 to 10.2 nm (Fig. S6c). The application of a negative V_G will push charge carriers towards the a-CZO/KTO(111) interface, leading to a higher degree of disorder. This reduction in ΔR_S cannot be explained by enhanced disorder, as the higher disorder induced by negative V_G generally results in increased resistance. The decrease in ΔR_S as V_G decreases could be attributed to reduced carrier density (Fig. S6c), which results in more sparsely distributed superconducting islands in a non-superconducting background. Consequently, the resistance effect induced by vortex motion across the weak links between superconducting grains is weakened.

To get the knowledge about the dynamic process, the magnetic hysteresis has been systemically explored by varying the sweep rate of $\mu_0 H_{||}$ for the 2DEG with $n_S = 4.3 \times 10^{13}$ cm^{-2}. As shown in Fig. 3c, the magnitude of the MR curve strongly depends on the field sweep rate, and rapidly increases with the increase of the sweep rate. As the sweep rate increases from 0.02 to 0.10 T/min, for example, the peak value grows from ~0.4 to ~19.6 Ω/□. At very slow sweep rates, the peak becomes minor and even negligible. Similar results have been reported for the superconducting LAO/STO interfaces, as the transport evidence for the coexistence of superconductivity and ferromagnetism[41,45]. As expected from our earlier discussion, the vortex motion generated by the dynamics of the ferromagnet during magnetization reversal leads to a sharp resistance peak. The rate at which the magnetic vortices are generated is proportional to the time dependence of the magnetization of the ferromagnet, and the rate of magnetization change is proportional to the sweep rate of external field. Therefore, the evolution of the R_S–$\mu_0 H_{||}$ loops with the sweep rate of the magnetic field provides conclusive proof that magnetization dynamics are responsible for the resistance peak when magnetic ordering and superconducting take place concomitantly.

Notably, the butterfly-shaped MR hysteresis is absent when measured with out-of-plane magnetic fields (Figs. 2a and S12). This result markedly contrasts with the behaviors of the superconducting 2DEG at the LAO/STO interface[41], where MR hysteresis is observed under both in-plane and out-of-plane magnetic fields, indicating the existence of Bloch-type domain walls. Alternatively, Néel domain walls may form at the interface, considering that the easy axis of the 2D magnetism is parallel to the a-CZO/KTO(111) interface. This can be confirmed by comparing the SQUID measurements of the in-plane and out-of-plane ferromagnetic hysteresis loops (Fig. S13). Unlike STO, the strong SOC of 5*d* Ta could cause magnetic anisotropy[21]. An in-plane easy magnetic axis alignment has also been observed in the $LaAlO_3$/KTO(111) and $YAlO_3$/KTO(111) systems[29]. The magnetization lies in the plane of the interface, and the in-plane external magnetic field is able to drive the movement of domain walls, whereas the out-of-plane external magnetic field is not. Therefore, the dependence of MR loops on the magnetic field direction is strongly influenced by the easy-plane anisotropy of magnetism. In our work, the absence of the out-of-plane MR hysteresis corroborates the in-plane easy axis of magnetization. Notably, a similar behavior has also been observed in the normal-state 2DEG at the EuO/KTO (110) interface[33]. Here, we would like to emphasize that although the magnetization configuration in the actual system during magnetic reversal may be far more complicated than that proposed here, the underlying mechanism is similar.

The vortices will be pinned by domain walls, and their motion is enabled by the domain wall reconfiguration driven by magnetic fields. As vortices move, they can cause the phase of the superconducting order parameter to shift locally. If a vortex moves across a narrow superconducting wire, for example, it can lead to a complete circle of phase change (0–2π or −2π to 0), which is termed a phase slip, i.e., the intrinsic fluctuations of the superconducting order parameter[46–54]. It is therefore necessary to get the information about phase slips in the process of superconducting transition. In general, thermally activated phase slips (TAPS) occur when thermal energy is higher than the energy barrier between two neighboring metastable states, enabling the system to overcome the energy barrier via thermal fluctuations. When the phase slip is thermally activated, it can be described by the formula of the Langer–Ambegaokar–McCumber–Halperin (LAMH) theory[47–49]:

$$R_{\mathrm{TAPS}} = \frac{\pi \hbar^2 \Omega}{2e^2 k_B T} \exp\left(-\frac{\Delta F(T)}{k_B T}\right) \tag{3}$$

where $\Delta F(T) = \frac{8\sqrt{2}}{3}\frac{H_C{}^2(T)}{8\pi} S \xi_{\mathrm{GL}}(T)$ is the energy barrier, $\Omega = \frac{L}{\xi_{\mathrm{GL}}(T)\tau_{\mathrm{GL}}}\left[\frac{\Delta F(T)}{k_B T}\right]^{1/2}$ is the attempt frequency, T_C^{zero} is the zero-resistance temperature, $\tau_{\mathrm{GL}} = \pi\hbar/8k_B(T_C^{\mathrm{zero}} - T)$ is the characteristic relaxation time in the time-dependent Ginzburg–Landau theory, $H_C(T) = H_C(0)\ (1 - T/T_C^{\mathrm{zero}})$ is the thermodynamic critical field, and $\xi_{\mathrm{GL}}(T) = \xi_{\mathrm{GL}}(0)(1 - T/T_C^{\mathrm{zero}})^{-1/2}$ is the Ginzburg–Landau coherence length. L is the length of the sample in the direction of the current, and S is the cross-sectional area of the sample. k_B is the Boltzmann constant and $\hbar$ is the reduced Planck constant. Another mechanism for the activation of phase slips is quantum tunneling below the free energy barrier triggered by quantum fluctuations, thus referred to as quantum phase slips (QPS). When thermal energy is insufficient to overcome the free energy barrier, quantum tunneling becomes the dominant mechanism. QPS were theoretically investigated by Golubev–Zaikin[51], and the temperature dependence of the resistance is given by refs. 50,51:

$$R_{\mathrm{QPS}}(T) = B_1 R_Q S_{\mathrm{QPS}} \frac{L}{\xi_{\mathrm{GL}}(T)} \exp(-S_{\mathrm{QPS}}) \tag{4}$$

where $S_{\mathrm{QPS}} = B_2\left(\frac{R_Q}{R_N}\right)\left(\frac{L}{\xi_{\mathrm{GL}}(T)}\right)$ is the effective action, B_1 and B_2 are constants, $R_Q = h/4e^2$ is the quantum resistance, and R_N is the normal state resistance.

A fingerprint of phase slips is the broadening of the superconducting transition process[48]. Therefore, we further analyzed the superconducting transition width (ΔT) for the samples with different doping levels, where ΔT is defined as $T(R_S = 0.8R_{4K}) - T(R_S = 0.2R_{4K})$. ΔT broadens from 0.12 to 0.32 K when n_S increases from 3.8×10^{13} to 9.8×10^{13} cm^{-2}. To verify the fluctuation origin of the broadening transition, we fit Eqs. (3) and (4) to the T–T_C dependence of the R_S/R_{4K} in the transition region, as depicted in Figs. 3d and S14. The solid lines and dashed lines represent the fits to the TAPS and QPS models, respectively. In fact, TAPS is dominant at the temperature near T_C, where thermal fluctuations are significant[55]. As shown by the solid curves in Fig. 3d, the TAPS model well reproduces the transition-induced rapid resistance drop near T_C for all samples. However, when $n_S > 5 \times 10^{13}$ cm^{-2}, a weakly temperature-dependent resistance tail appears at lower temperatures, deviating significantly from the TAPS model. As the temperature decreases further, the magnitude of the free energy barrier relative to $k_B T$ increases, leading to a rapid reduction in the thermal-activation rate[55]. As this rate becomes negligible, tunneling through the energy barrier starts to dominate. As shown by the black dashed lines in Fig. 3d, the resistance tail behavior in the lower temperature range is well captured by Eq. (4), indicating that the QPS model performs well where the TAPS model fails. As the temperature decreases, a crossover from TAPS to QPS occurs for highly doped samples. Therefore, all samples follow the TAPS model near T_C, while high-density samples undergo a TAPS-to-QPS transition as the temperature decreases. By comparing the transport behaviors under magnetic fields for samples with different n_S, we found that the high-n_S sample exhibits a shorter $\xi_{\mathrm{GL}}(0)$. Specifically, $\xi_{\mathrm{GL}}(0) = 61.63$ nm and 16.43 nm for $n_S = 3.8 \times 10^{13}$ and 8.9×10^{13} cm^{-2}, respectively. The reduced coherence length in high-n_S samples could enhance quantum fluctuations[53], which becomes more pronounced at lower temperatures, enabling the TAPS-to-QPS transition.

To rule out disorder as the dominant mechanism influencing the change in transition width, we further compare the dependencies of the mean free path l_{mfp} and the superconducting transition width ΔT

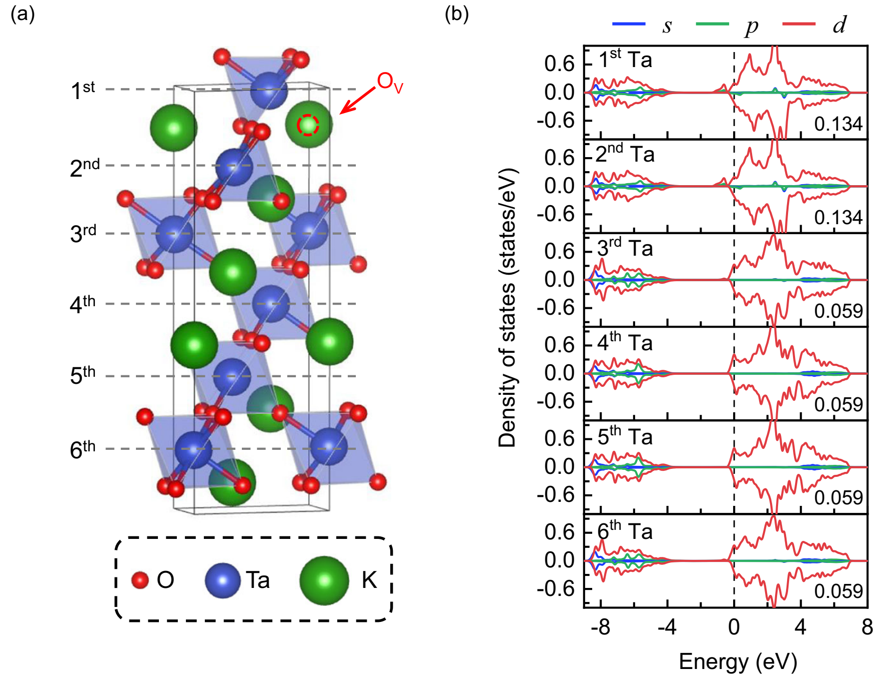

Fig. 4 | DFT calculations on KTO(111) layer structure. **a** Structural model of the KTO(111) layer with an oxygen vacancy at one KO_3 atomic layer for DFT calculation. **b** The orbital-resolved and layer-dependent density of states for the Ta atoms. Positive and negative densities of states represent the spin-up and spin-down states, respectively. Numbers in the figure indicate the net magnetization in the unit of μ_B/Ta.

on carrier density. As mentioned above, l_{mfp} does not exhibit a significant dependence on n_S (Fig. S11). However, the relationship of ΔT and carrier density indicates that the magnitude of ΔT is around ~0.12 K for low-n_S samples ($n_S < 5 \times 10^{13}$ cm^{-2}) but increases to about ~0.29 K for high-n_S samples ($n_S > 5 \times 10^{13}$ cm^{-2}). Obviously, the disorder mechanism fails to explain the obvious enhancement in ΔT as n_S exceeds 5×10^{13} cm^{-2}. However, this behavior is consistent with phase slips fitting results, that is, low-n_S samples only follow the TAPS model, while a TAPS-to-QPS transition occurs in high-n_S samples thus broadening the superconducting transition width. Therefore, the variation in transition width with carrier density is attributed to phase slips rather than disorder.

Given that the peak resistance ΔR_S of the hysteretic MR loop originates from the motion of magnetic vortices cross the weak links between superconducting islands, we further try to adopt the TAPS model to describe the strong-temperature dependence of the ΔR_S for the low-n_S sample in Fig. 2f. Although the LAMH theory is derived for the case of $\mu_0 H = 0$, it is applicable to the case with a finite magnetic field because the temperature dependence of both the energy barrier $\Delta F(T)$ and the coherence length $\xi_{GL}(T)$ has the same form as that of $\mu_0 H = 0$[56]. Therefore, we conduct a theoretical analysis of the ΔR_S–T relationship on the basis of the LAMH formula Eq. (3), adopting $\Delta R_S = R_{TAPS}(\mu_0 H_{||} = 0.08\ \mathrm{T}) - R_{TAPS}(\mu_0 H_{||} = 0)$. As illustrated in Fig. 2f, the fitting curve reproduces the main features of experimental data around T_C, indicating that the TAPS model captures the ΔR_S–T peak behavior close to T_C. Moreover, the validity of the TAPS model is also confirmed by the analysis of the dependence of peak resistance on both superconducting critical current and $\mu_0 H_{||}$ sweep rate, as detailed in Note 2 and Fig. S15. Therefore, it can be concluded that vortex motion can induce TAPS, which in turn affects the macroscopic properties of the superconductor and results in finite resistance. Notably, under an external magnetic field, vortex motion generated by magnetization dynamics is strongly influenced by the easy magnetic axis. In our work, the in-plane easy magnetic axis allows an in-plane external magnetic field to effectively drive magnetization dynamics, inducing vortex motion and phase slips, thereby generating a distinct hysteretic MR loop. In contrast, an out-of-plane external field, being orthogonal to the plane of magnetization rotation, is unable to drive magnetization dynamics. Consequently, the absence of the vortex motion implies that no phase slips occur, resulting in a lack of out-of-plane hysteretic behavior. Under a high initial positive in-plane magnetic field, the magnetic moment aligns with the applied field. As the field sweeps from positive to negative, the system retains its original magnetization even as the positive field decreases to zero. When the negative field approaches the coercive field, magnetic moment reversal occurs and magnetization dynamics will generate moving vortices that lead to phase slips, thereby resulting in finite resistance. Similarly, during a negative-to-positive sweep, magnetic moment reversal happens as the positive field reaches the coercive field. This explains the dependence of the resistance peak on the in-plane magnetic field sweep direction.

We summarize previous studies on upper critical field measurements of KTO(111) heterostructures[14,15,57,58], as detailed in Table S3. Notably, most of these studies have focused on interfaces with higher carrier densities, while a few studies involving low-carrier-density samples have only measured out-of-plane magnetoresistance. These factors might have impeded the observation of magnetotransport evidence that supports the coexistence of superconductivity and ferromagnetism at KTO(111) interfaces in earlier studies.

To elucidate the origin of the ferromagnetism that coexists with superconductivity, we performed DFT calculations for the KTO(111) layer structure as schematically shown in Fig. 4a (see detailed modeling in Methods). The constructed KTO(111) layer consists of six KTO unit cells with an oxygen vacancy at one KO_3 atomic layer (marked by the red dashed circle). Figure 4b shows the calculated orbital-resolved and layer-dependent DOS for the Ta atoms. Combined with the calculated band structures (Fig. S16), it can be concluded that the KTO(111) layer exhibits both metallic and magnetic properties, which coincides with our experimental observations. In Fig. 4b we presented the calculated magnetic moment per Ta atom and the layer-dependent polarization of the Ta 5*d* states. We can see that the ferromagnetism mainly arises from the first and second Ta atomic layers neighboring the oxygen vacancy, with the magnetic moment of ~0.13 μ_B/Ta. For Ta atoms located far from the oxygen vacancy, the calculated magnetic moments drop rapidly to ~0.059 μ_B/Ta. We further analyzed the orbital-resolved DOS for the Ta atoms and oxygen atoms around the oxygen vacancy (Fig. S17), and found that the ferromagnetism of Ta atoms is primarily contributed by the Ta $5d_{yz}$ orbital which partially hybridizes with the Ta $5d_{x^2-y^2}$ and O $2p_y$ orbitals. The layer-by-layer orbital-resolved DOS for the *d* orbitals from Ta atoms (Fig. S17b) indicates that the magnetism is mainly attributed to the Ta $5d_{yz}$ orbital in the first two TaO_2 layers. The real-space spin density $\Delta\rho = \rho_\uparrow - \rho_\downarrow$ is shown in Fig. S17c, and the spin-density isosurface near oxygen vacancy is mainly dominated by the spin-up Ta $5d_{yz}$ orbitals. In fact, a Ta–O_v–Ta dimer with an oxygen vacancy located between two Ta atoms is formed when an oxygen vacancy is introduced into one KO_3 atomic layer. Such absence of local covalent bonding and a reduction in local symmetry will strongly lower the energy of the *d* orbitals with lobes pointing to the vacancy[59]. As shown in Fig. S17c, the Ta d_{yz} orbital lies in the *yz* plane with lobes aligning along the Ta–O_v–Ta direction, which significantly lowers its energy. Consequently, electrons transferred from the oxygen vacancy preferentially occupy the lower-energy state, specifically the Ta d_{yz} orbital. The substantial spin splitting of the Ta d_{yz} orbital near the Fermi level introduces an asymmetry between spin-up and spin-down contributions, leading to spin polarization.

The DFT study reveals that specific orbitals are responsible for magnetism, which may open the door to exploring the origin of magnetism through orbital-selective spectroscopic techniques. Highly sensitive resonant X-ray techniques, such as X-ray magnetic circular dichroism, X-ray linear dichroism, and X-ray absorption spectroscopy, are particularly well-suited to provide further experimental evidence and shed light on the orbital selectivity of magnetism. We believe that our theoretical findings provide the foundation and guidance for future research employing orbital-selective spectroscopic techniques to verify the contribution of specific orbitals to magnetism in KTO-based 2DEGs.

The physical origin of ferromagnetism for the momentum-confined interacting 2DEG can be understood based on the Stoner model[60], where both Stoner parameter I_S and the DOS at the Fermi level in the nonmagnetic state $N(E_F)$ determine whether the system favors a ferromagnetic or paramagnetic state. I_S describes the strength of electron exchange, whereas $N(E_F)$ is inversely proportional to the kinetic energy of the electrons. The competition between the exchange and kinetic energy is taken into account by the Stoner criterion[61], according to which the system would be unstable at the nonmagnetic state if $N(E_F)I_S > 1$. The Stoner FM transition can reduce the total energy of the system and thus stabilize the FM state. As shown in Fig. S18, the total non-spin-polarized DOS at the Fermi level $N(E_F)$ is significantly enhanced by the oxygen vacancy-induced gap states, and a sharp DOS peak located at the Fermi level indicates a Stoner-type instability. The Stoner parameter I_S can be calculated through $I_S = \Delta\mu_B/M$, where Δ is the spin splitting energy and M is the magnetic moment per Ta atom. The calculated $N(E_F)$ and I_S are 7.0 state/eV and 1.4 eV, respectively. Obviously, the Stoner criterion $N(E_F)I_S = 9.8 > 1$ is satisfied. Therefore, the KTO(111) layer structure with oxygen vacancy-doped electrons has an FM ground state. In our spin-polarized calculations for the FM configuration, the DOS peak splits and shifts away from the Fermi level, with the calculated total energy of the FM state being 4 meV lower than that of nonmagnetic states. In the Stoner scenario, the magnetic strength in the normal state is expected to depend on the carrier density. The increase in saturation magnetization as n_S grows is confirmed by the magnetic data obtained at 2 K by the SQUID magnetometer (Fig. S19). Given that the carrier density increases with the number of oxygen vacancies, DFT calculations on the KTO(111) layer structure with two oxygen vacancies were performed (Fig. S20). When the number of oxygen vacancies increases from one to two, the DOS at the Fermi level $N(E_F)$ in normal state increases from 7 to 9.4 states/eV. Accordingly, the total net magnetization increases from 0.504 to 1.335 μ_B. Therefore, the experimental results, combined with theoretical calculations, suggest an enhancement in ferromagnetism as the carrier density increases, further validating the Stoner scenario.

Notably, the magnetic moments originate from the itinerant electrons which are relatively localized around the oxygen vacancy, and the conductivity is contributed by itinerant electrons which come from each Ta atomic layer. According to this scenario, both ferromagnetism and superconductivity occur involving the Ta 5*d* electrons. However, the electron layers that are responsible for magnetic ordering and superconducting have different spatial distributions, as the oxygen vacancies are more localized to the a-CZO/KTO(111) interface. The local imaging measurement using scanning SQUID enables direct visualization of landscapes of ferromagnetism, paramagnetism, and superconductivity[6,62]. In fact, Julie et al. have directly imaged the coexistence of ferromagnetism and superconductivity at the LAO/STO interface using scanning SQUID, providing evidence for nanoscale spatial phase separation[6]. Therefore, the coexistence of ferromagnetism and superconductivity at the oxide interface could generally be understood as the simultaneous presence of both magnetic and superconducting phases and does not necessarily imply a strict spatial overlap between the two phases. Nonetheless, this does not diminish the profound interplay between magnetism and superconducting pairing at the oxide interface, which plays a central role in determining the emergence of unconventional superconducting states.

Recent studies have revealed the emergence of superconducting stripes in EuO/KTO systems[15,33], induced by the ferromagnetic proximity effect of EuO. In our study, in-plane anisotropic transport behavior, a signature of superconducting stripes, was observed in the sample with $n_S = 4.3 \times 10^{13}\,cm^{-2}$ but was absent in the sample with $n_S = 8.9 \times 10^{13}\,cm^{-2}$ (Fig. S21). A similar n_S-dependent in-plane anisotropic superconducting behavior has also been observed at the EuO/KTO (110) interface[33].

As mentioned earlier, the superconductivity of 2DEGs at KTO interfaces is highly dependent on crystal orientation, with the T_C being highest at the (111) interface and lower at the (110) interface. No superconductivity is observed down to 25 mK at the (001) interface. Notably, the crystal orientation dependence of the coexistence of magnetism and superconductivity is also a compelling issue, which could be explored in the (111) and (110) orientations. Although the (111) orientation appears to be the most favorable for superconductivity, this does not necessarily imply that it also favors the coexistence of magnetism and superconductivity, especially given the inherent competition between magnetism and superconductivity. Therefore, due to the complex interplay between magnetism and superconductivity, the dependence of their coexistence on crystal orientation requires further investigations.

In summary, definite signatures for the coexistence of 2D superconductivity and ferromagnetism are observed in the 2DEGs at the nonmagnetic a-CZO/KTO(111) interfaces, as indicated by the appearance of remarkable MR hysteresis in the superconducting background. Butterfly-shaped MR is detected in a wide temperature range, from the onset temperature of the superconductivity down to extremely low temperatures where the system enters deeply into the superconducting state. Specifically, the magnitude of the MR peak is found to be strongly temperature dependent, small at the onset temperature, reaching a maximum value around the superconducting transition temperature, and small again at even lower temperatures. These features are well captured by the model of TAPS. Moreover, the magnitude of the MR strongly depends on the field sweep rate, growing rapidly as the sweep rate increases. This observation reveals the close relation between hysteretic MR and magnetization dynamics. Theoretical analysis shows that the magnetic moments originate from the itinerant electrons, which are relatively localized around the oxygen vacancy and mainly arise from the Ta $5d_{yz}$ orbital. The present work reveals the strong interplay between ferromagnetism and superconductivity, paving the way towards the exploration of quantum emergent phenomena.

Methods

Sample fabrication and characterization

Amorphous CZO films with the thickness of 10 nm were grown on (111)-oriented KTO single crystalline substrates by the technique of PLD with a ceramic CZO target. A KrF Excimer laser (wavelength is 248 nm) was employed. The repetition rate was 2 Hz and the fluence was ~2 J/cm^2. During the deposition process, the substrate temperature was kept at 300 °C, while the O_2 partial pressure P_{O2} varied from 7×10^{-3} to 1×10^{-5} Pa (details in Supporting Information). We obtained the 2DEGs at the a-CZO/KTO(111) interfaces with different doping levels, i.e., carrier densities. After deposition, the temperature of the sample was furnace-cooled to room temperature under the same atmosphere. Film thickness was determined by the number of laser pulses, which have been carefully calibrated by small-angle X-ray reflectivity. The surface morphology of the heterostructure was measured by atomic force microscope (AFM, SPI 3800N, Seiko). Lattice images were recorded by a high-resolution scanning transmission electron microscope (STEM) with double C_S correctors (JEOL-ARM200F). The samples have been patterned into the Hall bar configuration using standard optical lithography and argon etching techniques. The central Hall bar bridge is 20 μm in width and 120 μm in length. XPS was measured using an Al Kα source in a Thermo Scientific ESCALAB 250X system. The magnetic properties were measured by a Quantum-designed vibrating sample magnetometer scanning superconducting quantum interference device.

Electrical transport measurements

The transport measurements including R_S–T and Hall effect (temperature ranging from 300 to 2 K) were performed on a Quantum-designed physical properties measurement system. An applied current of 1 μA was used. The electrical transport measurements at lower temperature were conducted in a dilution refrigerator equipped with a vector-type magnet by a standard AC lock-in detection method. The AC excitation current of 10 nA at a frequency of 17.7777 Hz was applied using a Keithley 6221 current source. The corresponding AC voltage signals were measured using NF LI5650 lock-in amplifiers. For I–V curves measurements, a DC current was applied by Keithley 2400 and the corresponding voltage was measured using the same instrument. Ultrasonic wire bonding (Al wires of 20 μm in diameter) was used for electric connection. Unless specifically stated, Hall bar configuration was adopted to the measurements, the applied current direction is along [11-2] and the field sweep rate is 0.10 T/min.

Phase slips model

Superconductivity distinguishes itself by its remarkable ability to carry charge current with zero dissipation, which can be characterized by a macroscopic wave function $\Psi(r) = |\Psi(r)|e^{i\varphi(r)}$, termed the order parameter. The amplitude and phase coherence of the order parameter vanishes at the transition temperature where the system goes back to the normal phase. However, even below the critical temperature, the phase coherence of the system can be affected by the so-called phase slips, i.e., phase fluctuations of the order parameter, which induce a finite resistance and therefore lead to a destruction of persistent currents. A phase slip is an elementary excitation of the order parameter due to thermal or quantum fluctuations, corresponding to a local suppression of its amplitude and a simultaneous jump of the phase by 2π. A phase slip can be thermally activated when the temperature is higher than the free energy barrier $\Delta F(T)$ between two neighboring metastable states and the system may overcome the barrier via thermal fluctuations. Another mechanism for the activation of phase slips is quantum tunneling below the free energy barrier triggered by quantum fluctuations, thus referred to as QPS. According to the Arrhenius law[47,49], TAPS is extremely improbable for $T \le \Delta F(T)/k_B$. The prime fitting parameters used in the simulation of Eqs. (3) and (4) in Figs. 3c and S14, along with a comparison to experimental data, are listed in Table 1.

Table 1 | Summary of the prime fitting parameters in the phase slips model

n_S (10^{13} cm^{-2})	TAPS model		QPS model	Exp.
	T_C^{zero}	$\Delta F(0)$ (10^{-23} J)	T_C^{zero}	T_C^{zero}
3.8	0.60	5.18 ± 0.02	–	0.60
4.3	0.74	10.86 ± 0.03	–	0.74
5.8	0.80 ± 0.20	7.51 ± 0.05	0.80 ± 0.30	0.80
8.9	1.79 ± 0.13	26.53 ± 0.52	1.79 ± 0.16	1.79
9.8	1.86 ± 0.21	29.63 ± 0.20	1.86 ± 0.27	1.86

Density functional theory calculations

First-principles calculations were performed using the projector-augmented wave method within the DFT[63,64], as implemented in the Vienna Ab-initio Simulation Package[65,66]. To describe the exchange-correlation energy, we used the general gradient approximation with the Perdew-Burke-Ernkzerhof for solids parametrization[67,68]. The strong on-site Coulomb repulsion among Ta $5d$ electrons is corrected by using the DFT+U method, where U is the Hubbard parameter. The U_{eff} = 3 eV is used for Ta $5d$ states. In our computational investigation, the construction of a KTO(111) layer consists of six KTO unit cells with an oxygen vacancy at one KO_3 atomic layer for simulating the electronic and magnetic properties. Our convergence standard requires that the Hellmann-Feynman force on each atom is less than 0.01 eV/Å and the absolute total energy difference between two successive consistent loops is smaller than 10^{-5} eV. The KTO(111) layer was fully optimized using a Γ-centered $4\times4\times1$ k-grid, and the plane wave energy cutoff was set to 500 eV. The electronic structure calculations were performed by adopting a Γ-centered $9\times9\times1$ k-grid.

Data availability

The authors declare that data generated in this study are provided in the paper and the Supplementary Information file. Further datasets are available from the corresponding author upon request.

References

1. Reyren, N. et al. Superconducting interfaces between insulating oxides. *Science* **317**, 1196–1199 (2007).
2. Gozar, A. et al. High-temperature interface superconductivity between metallic and insulating copper oxides. *Nature* **455**, 782–785 (2008).
3. Wang, Q. Y. et al. Interface-induced high-temperature superconductivity in single unit-cell FeSe films on SrTiO3. *Chin. Phys. Lett.* **29**, 037402 (2012).
4. Ohtomo, A. & Hwang, H. A high-mobility electron gas at the LaAlO3/SrTiO3 heterointerface. *Nature* **427**, 423–426 (2004).
5. Li, L., Richter, C., Mannhart, J. & Ashoori, R. C. Coexistence of magnetic order and two-dimensional superconductivity at LaAlO3/SrTiO3 interfaces. *Nat. Phys.* **7**, 762–766 (2011).
6. Bert, J. A. et al. Direct imaging of the coexistence of ferromagnetism and superconductivity at the LaAlO3/SrTiO3 interface. *Nat. Phys.* **7**, 767–771 (2011).

7. Dikin, D. A. et al. Coexistence of superconductivity and ferromagnetism in two dimensions. *Phys. Rev. Lett.* **107**, 056802 (2011).
8. Monthoux, P., Balatsky, A. & Pines, D. Weak-coupling theory of high-temperature superconductivity in the antiferromagnetically correlated copper oxides. *Phys. Rev. B* **46**, 14803 (1992).
9. Lake, B. et al. Antiferromagnetic order induced by an applied magnetic field in a high-temperature superconductor. *Nature* **415**, 299–302 (2002).
10. Mukuda, H., Shimizu, S., Iyo, A. & Kitaoka, Y. High-Tc superconductivity and antiferromagnetism in multilayered copper oxides–A new paradigm of superconducting mechanism. *J. Phys. Soc. Jpn.* **81**, 011008 (2011).
11. Han, Y.-L. et al. Two-dimensional superconductivity at (110)LaAlO3/SrTiO3 interfaces. *Appl. Phys. Lett.* **105**, 192603 (2014).
12. Monteiro, A. et al. Two-dimensional superconductivity at the (111) LaAlO3/SrTiO3 interface. *Phys. Rev. B* **96**, 020504 (2017).
13. Mallik, S. et al. Superfluid stiffness of a KTaO3-based two-dimensional electron gas. *Nat. Commun.* **13**, 4625 (2022).
14. Zhang, G. et al. Spontaneous rotational symmetry breaking in KTaO3 heterointerface superconductors. *Nat. Commun.* **14**, 3046 (2023).
15. Liu, C. et al. Two-dimensional superconductivity and anisotropic transport at KTaO3(111) interfaces. *Science* **371**, 716–721 (2021).
16. Liu, C. et al. Tunable superconductivity and its origin at KTaO3 interfaces. *Nat. Commun.* **14**, 951 (2023).
17. Chen, Z. et al. Electric field control of superconductivity at the LaAlO3/KTaO3(111) interface. *Science* **372**, 721–724 (2021).
18. Zhang, H. et al. Unusual electric and optical tuning of KTaO3-based two-dimensional electron gases with 5d orbitals. *ACS Nano* **13**, 609–615 (2019).
19. Sun, Y. et al. Critical thickness in superconducting LaAlO3/KTaO3(111) heterostructures. *Phys. Rev. Lett.* **127**, 086804 (2021).
20. Chen, Z. et al. Two-dimensional superconductivity at the LaAlO3/KTaO3(110) heterointerface. *Phys. Rev. Lett.* **126**, 026802 (2021).
21. Hua, X. et al. Tunable two-dimensional superconductivity and spin-orbit coupling at the EuO/KTaO3(110) interface. *npj Quantum Mater.* **7**, 97 (2022).
22. Xu, H. et al. Giant tunability of Rashba splitting at cation-exchanged polar oxide interfaces by selective orbital hybridization. *Adv. Mater.* **36**, e2313297 (2024).
23. Buzdin, A. I. Proximity effects in superconductor-ferromagnet heterostructures. *Rev. Mod. Phys.* **77**, 935–976 (2005).
24. Qi, X., Hughes, T. L., Raghu, S. & Zhang, S. Time-reversal-invariant topological superconductors and superfluids in two and three dimensions. *Phys. Rev. Lett.* **102**, 187001 (2009).
25. Hasan, M. Z. & Kane, C. L. Colloquium: topological insulators. *Rev. Mod. Phys.* **82**, 3045–3067 (2010).
26. Linder, J. & Balatsky, A. V. Odd-frequency superconductivity. *Rev. Mod. Phys.* **91**, 045005 (2019).
27. Nakosai, S., Tanaka, Y. & Nagaosa, N. Topological superconductivity in bilayer Rashba system. *Phys. Rev. Lett.* **108**, 147003 (2012).
28. Wang, H. et al. Emergent superconductivity in topological-kagome-magnet/metal heterostructures. *Nat. Commun.* **14**, 6998 (2023).
29. Ning, Z. et al. Coexistence of ferromagnetism and superconductivity at KTaO3 heterointerfaces. *Nano Lett.* **24**, 7134–7141 (2024).
30. Saito, Y., Kasahara, Y., Ye, J., Iwasa, Y. & Nojima, T. Metallic ground state in an ion-gated two-dimensional superconductor. *Science* **350**, 409–413 (2015).
31. Halperin, B. I. & Nelson, D. R. Resistive transition in superconducting films. *J. Low. Temp. Phys.* **36**, 599–616 (1979).
32. Kozuka, Y. et al. Two-dimensional normal-state quantum oscillations in a superconducting heterostructure. *Nature* **462**, 487–490 (2009).
33. Hua, X. et al. Superconducting stripes induced by ferromagnetic proximity in an oxide heterostructure. *Nat. Phys.* **20**, 957–963 (2024).
34. Chandrasekhar, B. S. A note on the maximum critical field of high-field superconductors. *Appl. Phys. Lett.* **1**, 7–8 (1962).
35. Clogston, A. M. Upper limit for the critical field in hard superconductors. *Phys. Rev. Lett.* **9**, 266–267 (1962).
36. Uwe, H., Oka, K., Unoki, H. & Sakudo, T. Raman scattering from conduction electron in KTaO3. *J. Phys. Soc. Jpn.* **49**, 577–580 (1980).
37. Uwe, H., Sakudo, T. & Yamaguchi, H. Interband electronic raman scattering in SrTiO3. *Jpn. J. Appl. Phys.* **24**, 519 (1985).
38. King, P. D. C. et al. Subband structure of a two-dimensional electron gas formed at the polar surface of the strong spin-orbit perovskite KTaO3. *Phys. Rev. Lett.* **108**, 117602 (2012).
39. Gan, Y. et al. Light-induced giant Rashba spin–orbit coupling at superconducting KTaO3(110) heterointerfaces. *Adv. Mater.* **35**, 2300582 (2023).
40. Rout, P., Maniv, E. & Dagan, Y. Link between the superconducting dome and spin-orbit interaction in the (111)LaAlO3/SrTiO3 interface. *Phys. Rev. Lett.* **119**, 237002 (2017).
41. Mehta, M. et al. Evidence for charge–vortex duality at the LaAlO3/SrTiO3 interface. *Nat. Commun.* **3**, 955 (2012).
42. Zhang, H. et al. High-mobility spin-polarized two-dimensional electron gases at EuO/KTaO3 interfaces. *Phys. Rev. Lett.* **121**, 116803 (2018).
43. Zhang, H. et al. Thermal spin injection and inverse Edelstein effect of the two-dimensional electron gas at EuO-KTaO3 interfaces. *Nano Lett.* **19**, 1605–1612 (2019).
44. Jaeger, H., Haviland, D., Orr, B. & Goldman, A. Onset of superconductivity in ultrathin granular metal films. *Phys. Rev. B* **40**, 182 (1989).
45. Shen, S. et al. Observation of quantum Griffiths singularity and ferromagnetism at the superconducting LaAlO3/SrTiO3(110) interface. *Phys. Rev. B* **94**, 144517 (2016).
46. Kundu, H. K. et al. Effect of dimensionality on the vortex dynamics in a type-II superconductor. *Phys. Rev. B* **100**, 174501 (2019).
47. Langer, J. S. & Ambegaokar, V. Intrinsic resistive transition in narrow superconducting channels. *Phys. Rev.* **164**, 498–510 (1967).
48. Little, W. A. Decay of persistent currents in small superconductors. *Phys. Rev.* **156**, 396–403 (1967).
49. McCumber, D. & Halperin, B. Time scale of intrinsic resistive fluctuations in thin superconducting wires. *Phys. Rev. B* **1**, 1054–1070 (1970).
50. Zaikin, A. D., Golubev, D. S., van Otterlo, A. & Zimányi, G. T. Quantum phase slips and transport in ultrathin superconducting wires. *Phys. Rev. Lett.* **78**, 1552–1555 (1997).
51. Golubev, D. S. & Zaikin, A. D. Quantum tunneling of the order parameter in superconducting nanowires. *Phys. Rev. B* **64**, 014504 (2001).
52. Baumans, X. D. A. et al. Thermal and quantum depletion of superconductivity in narrow junctions created by controlled electromigration. *Nat. Commun.* **7**, 10560 (2016).
53. Sacépé, B., Feigel'man, M. & Klapwijk, T. M. Quantum breakdown of superconductivity in low-dimensional materials. *Nat. Phys.* **16**, 734–746 (2020).
54. Fisher, M. P. A. Vortex-glass superconductivity: a possible new phase in bulk high-Tc oxides. *Phys. Rev. Lett.* **62**, 1415–1418 (1989).
55. Giordano, N. Evidence for macroscopic quantum tunneling in one-dimensional superconductors. *Phys. Rev. Lett.* **61**, 2137 (1988).
56. Rogachev, A., Bollinger, A. T. & Bezryadin, A. Influence of high magnetic fields on the superconducting transition of one-dimensional Nb and MoGe nanowires. *Phys. Rev. Lett.* **94**, 017004 (2005).

57. Arnault, E. G. et al. Anisotropic superconductivity at KTaO3 (111) interfaces. *Sci. Adv.* **9**, eadf1414 (2023).
58. Liu, Y. et al. Superconductivity in epitaxially grown LaVO3/KTaO3 (111) heterostructures. *Chin. Phys. B* **32**, 037305 (2023).
59. Pavlenko, N., Kopp, T., Tsymbal, E., Mannhart, J. & Sawatzky, G. Oxygen vacancies at titanate interfaces: two-dimensional magnetism and orbital reconstruction. *Phys. Rev. B Condens. Matter Mater. Phys.* **86**, 064431 (2012).
60. Stoner, E. C. Collective electron ferromagnetism. *Proc. R. Soc. A* **165**, 372–414 (1938).
61. Zhuang, H. L., Kent, P. R. C. & Hennig, R. G. Strong anisotropy and magnetostriction in the two-dimensional Stoner ferromagnet Fe3GeTe2. *Phys. Rev. B* **93**, 134407 (2016).
62. Wang, X. et al. Multiferroicity in plastically deformed SrTiO3. *Nat. Commun.* **15**, 7442 (2024).
63. Hohenberg, P. & Kohn, W. Inhomogeneous electron gas. *Phys. Rev. B* **136**, B864–B871 (1964).
64. Kohn, W. & Sham, L. J. Self-consistent equations including exchange and correlation effects. *Phys. Rev.* **140**, A1133–A1138 (1965).
65. Kresse, G. & Joubert, D. From ultrasoft pseudopotentials to the projector augmented-wave method. *Phys. Rev. B* **59**, 1758–1775 (1999).
66. Blochl, P. E. Projector augmented-wave method. *Phys. Rev. B* **50**, 17953–17979 (1994).
67. Perdew, J. P., Burke, K. & Ernzerhof, M. Generalized gradient approximation made simple. *Phys. Rev. Lett.* **77**, 3865–3868 (1996).
68. Perdew, J. P. et al. Restoring the density-gradient expansion for exchange in solids and surfaces. *Phys. Rev. Lett.* **100**, 136406 (2008).

Acknowledgements

This work has been supported by the Science Center of the National Science Foundation of China (Grant No. 52088101(B.G.S.), and No. 52388201 (J.S.Z.)), the National Key Research and Development Program of China (Grant No. 2022YFA1403302 (J.R.S.), No. 2024YFA1410200 (H.Z.), No. 2021YFA1400300 (B.G.S.), No. 2021YFB3501200 (F.X.H.), No. 2021YFB3501202 (F.X.H.), No. 2023YFA1406003 (F.X.H.), and No. 2024YFA1409100 (J.S.Z.)), the National Natural Science Foundation of China (Grant No. 12474103 (H.Z.), No. T2394470 (W.S.Z. and H.Z.), No. T2394474 (W.S.Z. and H.Z.), No. 12274443 (J.R.S.), No. 12350404 (J.S.Z.), No. 12274252 (J.S.Z.), No. 92263202 (F.X.H.), No. U23A20550 (F.X.H.), and No. 22361132534 (F.X.H.)), the Strategic Priority Research Program B of the Chinese Academy of Sciences (Grant No. XDB33030200 (B.G.S.)), the Innovation Program for Quantum Science and Technology (Grant No. 2021ZD0302502 (J.S.Z.)), and the Beijing Outstanding Young Scientist Program (W.S.Z.).

Author contributions

H.Z. and J.S.Z. conceived the research project. H.Z., J.R.S., W.S.Z., and J.S.Z. designed the experiments; Y.N.X., D.M.T., W.J.Q., and D.Y.Z. prepared the samples; Y.N.X., Q.X.G., S.Y.Z., and Y.C.W. performed the transport measurements; Y.N.X. and M.Q.W. performed the magnetic property measurements; N.W. and B.G.L. performed the first-principles calculation; H.Z., Y.N.X., L.C., J.E.Z., F.R.H., H.W.Y., Y.S.C., F.X.H., B.G.S. and J.R.S. analyzed the data; H.Z., Y.N.X., and J.R.S. wrote the manuscript with input from all authors. These authors contributed equally: H.Z., Y.N.X., Q.X.G., and N.W.

Competing interests

The authors declare no competing interests.

Additional information

Supplementary information The online version contains supplementary material available at https://doi.org/10.1038/s41467-025-58300-9.

Correspondence and requests for materials should be addressed to Hui Zhang, Jirong Sun, Weisheng Zhao or Jinsong Zhang.

Peer review information *Nature Communications* thanks Avraham Klein, and the other, anonymous, reviewers for their contribution to the peer review of this work. A peer review file is available.

[1]School of Integrated Circuit Science and Engineering, Beihang University, Beijing, China. [2]State Key Laboratory of Low Dimensional Quantum Physics, Department of Physics, Tsinghua University, Beijing, China. [3]Beijing Institute of Nanoenergy and Nanosystems, Chinese Academy of Sciences, Beijing, China. [4]School of Nanoscience and Engineering, University of Chinese Academy of Sciences, Beijing, China. [5]Beijing National Laboratory for Condensed Matter Physics and Institute of Physics, Chinese Academy of Sciences, Beijing, China. [6]School of Physical Sciences, University of Chinese Academy of Sciences, Beijing, China. [7]Songshan Lake Materials Laboratory, Dongguan, Guangdong, China. [8]Ningbo Institute of Materials Technology & Engineering, Chinese Academy of Sciences, Ningbo, Zhejiang, China. [9]School of Physics, Zhejiang University, Hangzhou, Zhejiang, China. [10]Frontier Science Center for Quantum Information, Beijing, China. [11]Hefei National Laboratory, Hefei, Anhui, China. [12]These authors contributed equally: Hui Zhang, Yinan Xiao, Qixuan Gao, Ning Wu. e-mail: huizh@buaa.edu.cn; jrsun@iphy.ac.cn; wszhao@buaa.edu.cn; jinsongzhang@mail.tsinghua.edu.cn